

ARTICLE OPEN

Magneto-transport in inverted HgTe quantum wells

Ivan Yahnuk¹, Sergey S. Krishtopenko^{2,3}, Grzegorz Grabecki⁴, Benoit Jouault², Christophe Consejo², Wilfried Desrat², Magdalena Majewicz⁴, Alexander M. Kadykov², Kirill E. Spirin³, Vladimir I. Gavrilenko^{3,5}, Nikolay N. Mikhailov⁶, Sergey A. Dvoretzky^{6,7}, Dmytro B. But¹, Frederic Teppe², Jerzy Wróbel^{4,8}, Grzegorz Cywiński¹, Sławomir Kret⁴, Tomasz Dietl^{4,9,10} and Wojciech Knap^{1,2}

HgTe quantum wells (QWs) are two-dimensional semiconductor systems that change their properties at the critical thickness d_c , corresponding to the band inversion and topological phase transition. The motivation of this work was to study magnetotransport properties of HgTe QWs with thickness approaching d_c , and examine them as potential candidates for quantum Hall effect (QHE) resistance standards. We show that in the case of $d > d_c$ (inverted QWs), the quantization is influenced by coexistence of topological helical edge states and QHE chiral states. However, at $d \approx d_c$, where QW states exhibit a graphene-like band structure, an accurate Hall resistance quantization in low magnetic fields ($B \leq 1.4$ T) and at relatively high temperatures ($T \geq 1.3$ K) may be achieved. We observe wider and more robust quantized QHE plateaus for holes, which suggests—in accordance with the “charge reservoir” model—a pinning of the Fermi level in the valence band region. Our analysis exhibits advantages and drawbacks of HgTe QWs for quantum metrology applications, as compared to graphene and GaAs counterparts.

npj Quantum Materials (2019)4:13; <https://doi.org/10.1038/s41535-019-0154-3>

INTRODUCTION

Mercury cadmium telluride ($\text{Hg}_{1-x}\text{Cd}_x\text{Te}$) zinc-blende compounds are an example of rare semiconductor materials that form alloys over the whole composition range x while keeping the same crystal structure and the virtually unaltered lattice parameters.^{1,2} Accordingly, it is possible to tune the band structure by changing x and grow bulk films, two-dimensional (2D) quantum wells (QWs) or superlattices without strain-related material degradation. In this sense, $\text{Hg}_{1-x}\text{Cd}_x\text{Te}$ crystals are similar to the well-known $\text{Ga}_{1-x}\text{Al}_x\text{As}$ semiconductors, but show a much larger energy bandgap tunability, with band gaps ranging from $E_g \equiv E_{\Gamma_6} - E_{\Gamma_8} = 1.6$ eV for CdTe to the inverted band ordering, with $E_g = -0.30$ eV for HgTe at 4.2 K.¹ This peculiar aspect of $\text{Hg}_{1-x}\text{Cd}_x\text{Te}$ allows to reach $E_g \approx 0$ eV,^{2–4} and the conditions for observation of 3D carriers with massless Dirac-like linear dispersion and with high values of room- and low-temperature electron mobilities reaching 3.5×10^4 and 2×10^6 $\text{cm}^2 \text{V}^{-1} \text{s}^{-1}$, respectively.⁵ Moreover, since it is possible to adjust the bandgap below 100 meV, $\text{Hg}_{1-x}\text{Cd}_x\text{Te}$ -based systems are broadly employed in infrared and terahertz detectors,⁶ cameras,⁷ and lasers.⁸

Recent technological advances in molecular beam epitaxy (MBE) of $\text{Hg}_{1-x}\text{Cd}_x\text{Te}$ -based quantum structures have opened new and striking possibilities. In particular, HgTe/(Cd,Hg)Te QWs have allowed the demonstration of the existence of various topological phases in condensed matter.^{9–11} By changing the QW widths, the barrier alloy composition and the number of coupled QWs, it has been possible to demonstrate 2D topological insulators with 1D edge conducting channels^{12,13} as well as structures with band dispersions similar to single layer¹⁴ or bilayer graphene.¹⁵

Taking into account that $\text{Hg}_{1-x}\text{Cd}_x\text{Te}$ -based quantum structures have already broad commercial applications in night/thermal vision cameras and photonics,¹⁶ and that the MBE-grown HgTe QWs show a potential as a new generation of infrared and THz detectors,¹⁷ it is of interest determining structure layouts and experimental conditions under which the magnitude of Hall resistance can assume accurately quantized values, and to consider a potential of this material system for the quantum Hall effect (QHE) resistance standards.

QHE resistance standards make use of the accurate QHE quantization of the Hall resistance given by $\rho_{xy} = h/ie^2$, where i is an integer, and h and e are the Planck constant and the electron charge, respectively.^{18,19} Since their discovery,¹⁸ QHE standards have become a highly important tool in quantum metrology and are widely used in many national/international standardization institutions today.^{20–23} Currently, many materials are used for QHE standards. Despite differences in the material band structure, the sample imperfections and the geometry, unbelievably precise and wide Hall resistance plateaus are observed, independent of the host material, with a precision at the level going up to a few parts in 10^{10} (refs^{21–23}).

However, all currently used resistance standards operate at stringent experimental conditions: high magnetic fields B (requiring the use of superconducting coils) or extremely low temperatures T (requiring often the use of dilution³He refrigerators) (see Fig. 1). For example, typically, $B = 10$ T and $T = 1.5$ K for the GaAs-based standards. Recently, using the anomalous QHE resistance²⁴ of a ferromagnetic topological insulator, the feasibility of QHE resistance standards without

¹International Research Centre CENTERA, Institute of High Pressure Physics, Polish Academy of Sciences, 01-142 Warsaw, Poland; ²Laboratoire Charles Coulomb, University of Montpellier and CNRS UMR 5221, 34950 Montpellier, France; ³Institute for Physics of Microstructures, Russian Academy of Sciences, 603950 N. Novgorod, Russia; ⁴Institute of Physics, Polish Academy of Sciences, 02-668 Warsaw, Poland; ⁵Lobachevsky University, 603950 N. Novgorod, Russia; ⁶Rzhanov Institute of Semiconductor Physics, Siberian Branch of Russian Academy of Sciences, 630090 Novosibirsk, Russia; ⁷Tomsk State University, 634050 Tomsk, Russia; ⁸Faculty of Mathematics and Natural Sciences, University of Rzeszów, 35-959 Rzeszów, Poland; ⁹International Research Centre MagTop, Institute of Physics, Polish Academy of Sciences, 02-668 Warsaw, Poland and ¹⁰WPI-Advanced Institute for Materials Research, Tohoku University, Sendai 980-8577, Japan

Correspondence: Tomasz Dietl (dietl@MagTop.ifpan.edu.pl) or Wojciech Knap (knap.wojciech@gmail.com)

Received: 27 September 2018 Accepted: 1 April 2019

Published online: 23 April 2019

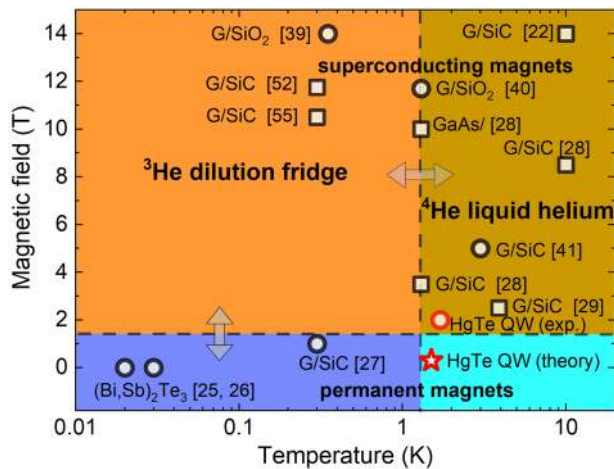


Fig. 1 Performances of several quantum Hall effect (QHE) standards presented as a function of magnetic field and temperature. Squares: demonstrated QHE standards (relative precision better than 10^{-9}) based on graphene and GaAs/GaAlAs quantum wells. Black circles: proof of concepts (relative precision below 10^{-8}) of QHE standards based either on graphene with permanent magnet or ferromagnetic materials. Red circle and star: the experimental result and theoretical predictions of this work. The cyan region is the only one accessible for both permanent magnets and liquid helium systems

applying a magnetic field ($B=0$ T) was demonstrated.^{25,26} In addition, QHE was observed in epitaxial graphene with ≈ 1 T permanent magnets.²⁷ However, both experiments required extremely low temperatures of ≈ 300 mK, provided only by ^3He refrigerators. The less stringent QHE standard metrology conditions ($B \approx 3.5$ T and $T \approx 1.3$ K²⁸) or ($B > 2.5$ T and $T \approx 3.8$ K²⁹) were recently achieved in epitaxial graphene. This was enabled by the very large LL splitting related to the hosting of massless Dirac fermions by the specific graphene band structure.^{30,31} Unfortunately, suitable metrological devices were obtained only by using graphene layers deposited on SiC substrates (G/SiC), with the mobility values restricted to $10^4 \text{ cm}^2 \text{ V}^{-1} \text{ s}^{-1}$, which limited metrological applications to magnetic fields higher than 2.5 T. Furthermore, because the G/SiC surface is usually covered by resist,^{29,32} the device properties degrade with time.³³ Therefore, the quest for better standards is still ongoing.

Due to the recent progress in molecular beam epitaxy (MBE), (Cd,Hg)Te-based QWs with a low carrier concentration and a very high carrier mobility can be grown, allowing for the observation of quantum limit $\nu=1$ conditions in magnetic fields below 1 T.³⁴ In addition, QHE in HgTe QWs with graphene-like band structures¹⁴ was observed even at liquid nitrogen temperatures.^{35,36} These findings show that HgTe/(Cd,Hg)Te QWs are promising candidates for use in QHE metrology.

In Fig. 1, we compare performances of several QHE resistance standards presented as a function of magnetic field and temperature. Squares correspond to QHE standards that reached the relative precision equal or better than 10^{-9} based on graphene and GaAs/GaAlAs quantum wells. Black circles: proof of concepts (relative precision below 10^{-8}) of QHE standards based either on graphene with permanent magnet or ferromagnetic materials. The dashed lines mark the limit of magnetic field and temperature related technological barriers: superconducting magnets and ^3He / ^3He / ^4He dilution refrigerators correspondingly. For the dissemination of the resistance standards in wider markets, new standards should be developed that can operate at magnetic fields allowing the usage of permanent magnets and at temperatures allowing the use of liquid helium (^4He) coolers. The cyan color region in Fig. 1 marks the range accessible for both permanent magnets³⁷ and liquid ^4He systems.³⁸

One has to mention, however, that the data in Fig. 1 concerns only magnetic field and temperature magnitudes (cryomagnetic conditions) of QHE standards.^{39–41} Of course, in practical applications, other factors have to be taken into consideration, such as a minimum time of the measurement to achieve the required accuracy (determined by signal to noise ratio that improves with the magnitude of breakdown current), the mastering and reproducibility of processing, metallization and packing, long term stability of the device, and its cost.^{20–22,39–41}

The main objective of this work is study magnetotransport properties of HgTe/(Cd,Hg)Te QWs in their different topological phases, determine importance of topological helical edge conduction and to examine different QWs from the point of view of their potential applications for QHE resistance standards. Our work is motivated by possibility of growth of QWs with (i) graphene-like band structure (large Landau Level splitting) and (ii) very high mobility carriers as well as (iii) developed device fabrication techniques, ensuring nowadays successful.

In this work, we experimentally and theoretically demonstrate that HgTe/(Cd,Hg)Te QWs with the thicknesses close to the critical value d_c and trivial band ordering, eliminating coexistence of conducting topological helical edge states together with QHE chiral states, allows reaching very favorable cryomagnetic conditions for the QHE resistance standards operation: low enough magnetic fields enabling use of permanent magnets ($B \leq 1.4$ T) simultaneously with liquid ^4He coolers (temperatures of $T \geq 1.3$ K) —reaching the cyan region in Fig. 1.

RESULTS

Investigated structures

Quantum structures were grown by MBE on GaAs (013) substrates.¹⁷ Three samples S1, S2, and S3, containing HgTe QWs with the thicknesses and barrier compositions of 7.1 nm, 8.0 nm, HgTe/Cd_{0.62}Hg_{0.38}Te, and 6.5 nm, HgTe/Cd_{0.65}Hg_{0.35}Te, respectively, have been studied. Measurements were performed on lithographically defined Hall bars with the dimensions of $L \times W = 80 \times 20 \mu\text{m}^2$, and $L \times W = 40 \times 20 \mu\text{m}^2$ (samples S1 and S2, respectively) and $L \times W = 650 \times 50 \mu\text{m}^2$ (sample S3). In addition, samples S2 and S3 had a top gate electrode allowing for carrier density control.⁴²

Figure 2a, b shows the layer sequence scheme and high-resolution electron microscopy (HREM) images of the cross section of sample S1. A perfect alignment of the successive atomic layers with the well-defined HgTe QW can be seen in Fig. 2b. Such high growth quality is crucial for obtaining the appropriate carrier mobility of HgTe QWs for QHE standards and can be reached only by the MBE growth technique.

Contribution of the TI states in QHE measurements

Most of the magnetotransport experiments were performed using the 8 T superconducting magnet system and standard lock-in measurement techniques. High-precision resistance measurements were performed using an HP3458A multimeter. The longitudinal and transverse resistances $\rho_{xx}(B)$ and $\rho_{xy}(B)$ for sample S1 are shown in Fig. 3a. The data correspond to $T = 1.7$ K, the hole concentration of $3.4 \times 10^{10} \text{ cm}^{-2}$ and mobility of $14.9 \text{ m}^2 \text{ V}^{-1} \text{ s}^{-1}$. A well-developed QHE plateau is visible already at $B \approx 0.7$ T. However, the ρ_{xy} quantization is not exact, and ρ_{xx} does not go to zero.

In the search for the origin of this parasitic ρ_{xx} conductivity, we consider the possibility of conduction through topological insulator 1D edge channels, as shown schematically in the inset of Fig. 3b.

We calculate the band structure and Landau Levels (LLs) fan charts for samples S1–S3 using the eight-band $k \cdot p$ Hamiltonian,⁴³ including the Γ_6 , Γ_8 , and Γ_7 bands of bulk materials and strain

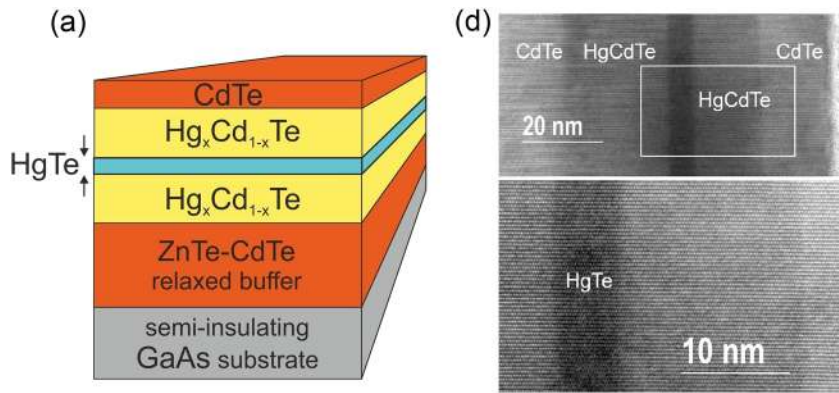


Fig. 2 **a** Schematic view of the layer sequence for MBE-grown HgTe/(Hg,Cd)Te QW structures. **b** High-resolution electron microscopy images of the structure cross section

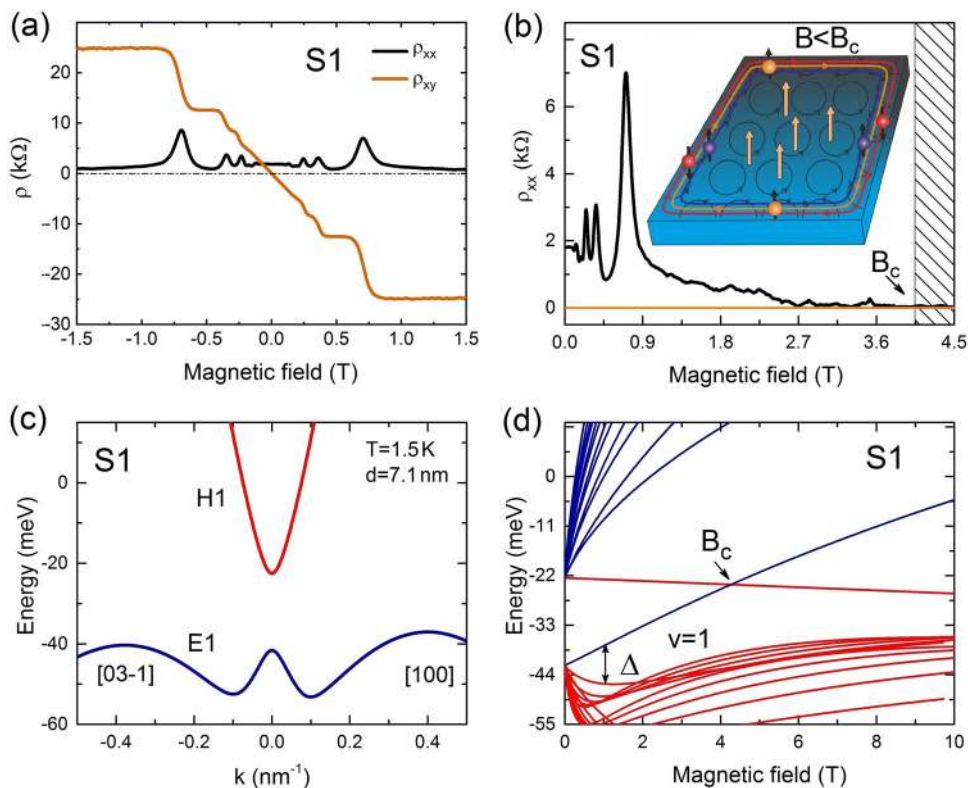


Fig. 3 **a** Magnetic field dependence of the Hall resistance ρ_{xy} and longitudinal resistance ρ_{xx} for holes in sample S1 with the inverted band structure. **b** $\rho_{xx}(B)$ for sample S1 in a wider magnetic field range. The inset shows schematic drawing of the coexistence of helical quantum spin Hall edge states (blue and red lines) with a conventional chiral quantum Hall state (orange line). **c** Calculated energy dispersion and **d** Landau levels as a function of the magnetic field for sample S1

effects due to lattice constant mismatch, with the parameters confirmed by our earlier investigations.^{44,45} According to the calculation results presented in Fig. 3, sample S1 has an inverted band structure up to the critical magnetic field $B_c \approx 4$ T, at which a crossing of the highest LL from the valence band with the lowest LL from the conduction band occurs.^{46,47} Interestingly, ρ_{xx} tends to be zero precisely when the magnetic field approaches $B_c \approx 4$ T (see Fig. 3b). This suggests that the existence of the inverted band structure and the related topological gap are detrimental to good quantization. It is possible that the combination of both counter-propagating topological edge states and disorder promotes backscattering beyond the expected topological gap. Supporting

this view results proving that the 1D edge conducting channels are indeed active even when the Fermi level is located beyond the topological gap have been obtained in the previous work.⁴⁸

To further explore conduction through the edge channels, we have investigated sample S2, which was equipped with a top gate controlling the carrier type and density. This sample also has an inverted band structure similar to sample S1, but with a slightly larger negative energy gap.

Well-developed quantum resistance plateaus $\rho_{xy} = \pm h/e^2$ were observed at magnetic fields starting from above ≈ 2 T for electrons and above ≈ 5.5 T for the holes, as illustrated in Fig. 4a and the 2D map in Fig. 4b. The edge state conduction is revealed by the

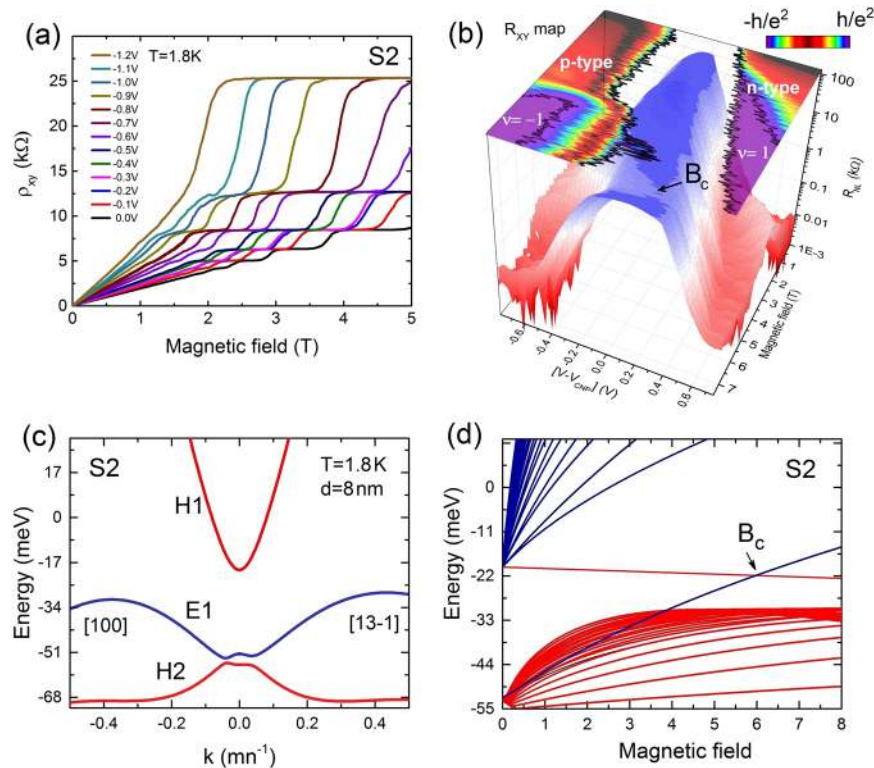


Fig. 4 **a** Hall resistivity for different carrier concentrations, controlled by the gate. **b** Dependence of the nonlocal resistance on the gate voltage and magnetic field for sample S2 (three-dimensional plot) and Hall resistance map (two-dimensional surface) showing regions of QHE for electrons ($\nu = 1$), holes ($\nu = -1$). **c** Calculated energy dispersion and **d** Landau level positions as a function of the magnetic field for sample S2

results of the nonlocal resistance measurements,⁴⁹ as shown in the 3D plot in Fig. 4b. Configuration of the nonlocal measurements presented in supplementary materials (see Fig. S1). The value of R_{NL} is plotted on the logarithmic scale to better visualize the residual edge conducting channels extending up to the QHE regions. As shown in Fig. 4 the resistance becomes very large when the Fermi level lies in the topological gap and decreases for magnetic fields higher than the critical value ($B_c \approx 6$ T for sample S2). As can be seen, in spite of the nonlocal resistance has its maximum for the Fermi level close to the charge neutrality point, the nonlocality still persists for the Fermi levels located in the band—far from the gap, extending to the QHE regions, as shown by the 2D map plotted above the 3D nonlocal resistance graph (Fig. 4b).

The existence of the critical field B_c , separating topological and non-topological phases, is a specific feature of charge transport in the inverted bandgap region of HgTe quantum wells. This feature has recently been explored to trace topological phase transition as a function of temperature.⁴⁴

6.5 nm QW in a magnetic field

Based on results presented above, we conclude that HgTe QWs with the smallest possible B_c should be engineered to decrease or avoid topological edge states perturbing the precision of the QHE. Figure 5 shows the band structure of sample S3. This sample has the smallest gap, and the smallest critical magnetic field of the three investigated samples, $B_c \approx 1.7$ T. The magnetoresistance data for sample S3 are shown in Fig. 5. On the electron side ($V_g = -1.2$ V, $\mu = 5$ m² V⁻¹ s⁻¹, panel c), the $\nu = 1$ plateau is observed above 1.5 T. The longitudinal resistance ρ_{xx} is < 0.1 Ω in $B = 2.5$ T, and $R_H = 25,807 \pm 7$ Ω , yielding the relative accuracy in the range of $\Delta R_H/R_K \approx (-2 \pm 3) \times 10^{-4}$.

On the hole side ($V_g = -2.5$ V, $\mu = 20$ m² V⁻¹ s⁻¹, panel d), the QHE is observed at a very low magnetic field $B \approx 0.5$ T. However, there is a small residual contribution $\rho_{xx} \approx 20$ Ω at this field, which we attribute to the counter-propagating topological edge states. Indeed, this residual resistivity decreases with magnetic field and is finally strongly suppressed, dropping to < 0.1 Ω around $B \approx 2$ T. Band structure calculations show that (similarly to the S1 and S2 samples) this field corresponds to the crossing of the conduction and valence band levels as well, signifying the transition from the inverted to the trivial band structure ($B \approx 1.7$ T, Fig. 5b).

In Fig. 5c, d, we show $\rho_{xx}(B)$ and $\rho_{xy}(B)$ for HgTe QWs with similar electron and hole densities adjusted by the gate voltage, whereas Fig. 5e presents a contour plot of σ_{xy} over a wide field and carrier density range. One can clearly see that the quantized value corresponding to $\nu = 1$ appears at a lower magnetic field for holes than in the n-type case. Also the QHE plateau is wider for holes. These facts can be attributed to the Fermi level pinning in the valence band region by a charge reservoir located either at QW or oxide interfaces. In fact, the charge transfer between interface states and the conducting channel is often considered as a complementary or a competing process to the well-known localization mechanism accounting for a non-zero width of QHE plateaus.⁵⁰ Such reservoir-related effects have also been observed in G/SiC, in which a surprisingly long plateau for $\nu = 2$ is assigned to the presence of interfacial charges residing between graphene and the SiC substrate.^{33,51,52} However, in the case of the QHE of holes in HgTe QWs, it is still not clear what is the role played by side maxima in the energy dispersion of the valence subband depicted in Fig. 5a. It is worth stressing that independently of underlining mechanism, our experimental observations show that for metrology applications slightly p-type doped non-topological HgTe QW's should be used.

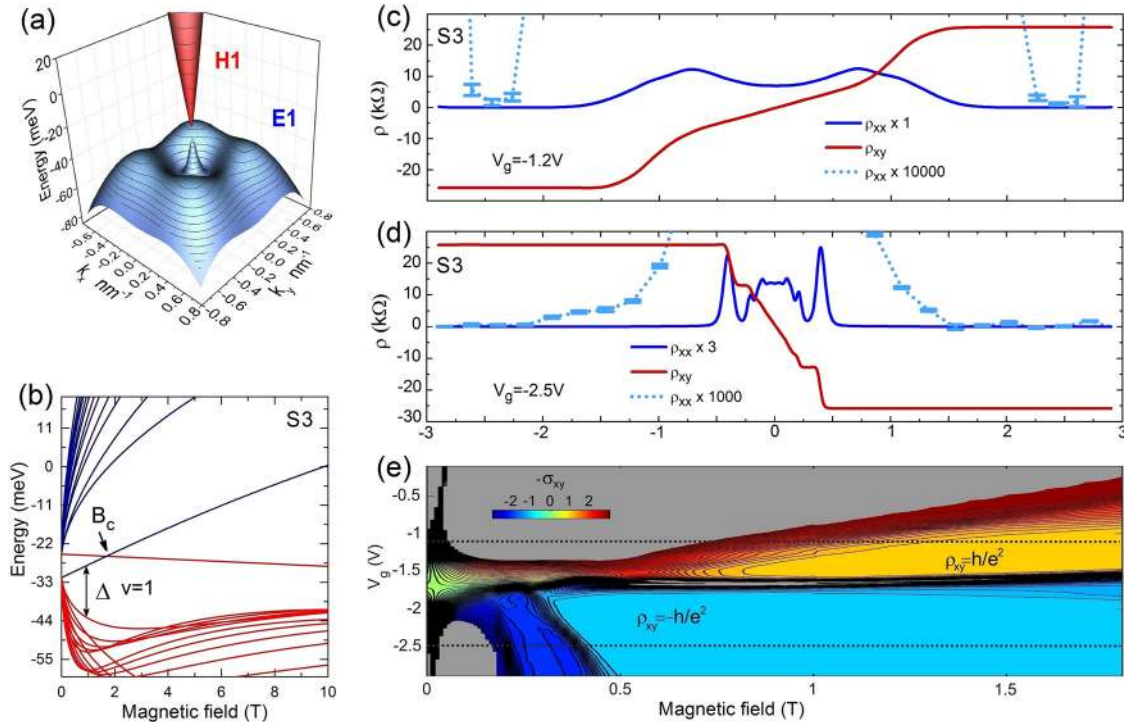


Fig. 5 **a, b** Calculated energy dispersion and Landau levels as a function of the magnetic field for sample S3. Quantum Hall effect in sample S3 at 1.7 K for two gate voltages: **c** corresponds to Fermi level in the conduction band, **d** corresponds to Fermi level in the valence band. Light-blue dotted lines represent magnified $\rho_{xx}(B)$ at the minima. **e** Hall conductivity as a function of magnetic field for different Fermi level positions controlled by the gate voltage. QHE plateaus at $\nu = 1$ correspond to yellow and cyan areas for electrons and holes, respectively

Summing all the R_H values collected between $1.8 < B < 3$ T at $I_{dc} = \pm 1$ μ A, we obtain $\Delta R_H/R_K \approx (3 \pm 30) \times 10^{-5}$. To further increase the overall precision, it would be mandatory to fabricate the QWs with smaller width (non-inverted band structure). Also sample geometry and contacts technology should be improved to maximize the magnitude of the breakdown current (see Discussion below).

Strain engineering for metrology applications

The results presented above show that good quantization precision at fields close to 0.5 T can be obtained by material engineering (slightly narrower QWs with the non-inverted band structure, $B_c \approx 0$ T). Further improvements in the QHE metrological conditions, i.e., lowering the operating magnetic field and increasing the temperature can be obtained in the QWs with higher Fermi velocity v_F . This velocity is determined by the slope of the linear energy dispersion, and its rise increases the energy spacing between the LLs. Recently, it has been experimentally demonstrated that the use of CdTe-Cd_{0.5}Zn_{0.5}Te strained-layer superlattices on GaAs as virtual substrates with an adjustable lattice constant allows effective control of the biaxial strain in the HgTe QWs from tensile ($\epsilon < 0$, $\epsilon \approx -0.32\%$ for CdTe buffer) to compressive ($\epsilon > 0$, up to $+1.40\%$).⁵³ Following this idea, we have performed calculations of the critical width d_c and the Fermi velocity v_F for the QWs with 2D massless Dirac fermions ($B_c = 0$ T) at different strains and at temperatures up to 100 K.

The calculations were made for the QWs grown along the (001) direction. It is worth noting, however, that the results for the (013) QWs are qualitatively the same.^{43,54} The calculated low-temperature (~ 1.5 K) energy dispersions, for two HgTe QWs hosting massless Dirac fermions for strain $\epsilon = -0.32\%$ (CdTe buffer) and $\epsilon = 1.3\%$, are shown in Fig. 6a and b. One should notice that the critical width d_c is different for these two structures: $d_c = 6.4$ nm and $d_c = 4.6$ nm, respectively. In Fig. 6c

we show the critical QW width d_c as a function of strain and temperature. One can see that with increase of temperature from 1 to 100 K, the critical width d_c increases by about 30%. It can be also seen (Fig. 6e) that the compressive strain indeed leads to an increase of the Fermi velocity (v_F) of the 2D massless Dirac fermions. Note that energy difference between the position of the side maxima into the valence band and charge neutrality point also raise with strain enhancement (see Fig. S2 in supplementary materials). Results presented in Fig. 6 indicate the ways of HgTe QWs engineering, in view of their applications for resistance standards.

To illustrate the advantages of HgTe QWs as the QHE resistance standards, in Fig. 6, we compare the energy spacing between the LLs (Δ) at the quantum limit conditions ($\nu = 1$) for G/SiC, GaAs/(Al, Ga)As QWs and the investigated HgTe/(Cd,Hg)Te QWs. It is conventionally assumed that thermal excitations cease to be relevant for metrological applications for $\Delta \geq 100k_B T$, corresponding to $\Delta \geq 13$ meV at $T = 1.5$ K. The second condition is $\mu B > 1$, where μ is the carrier mobility that determines the degree of the LL energy broadening. Both conditions, $\mu B > 1$ and $\Delta \geq 100k_B T$, merge together, defining the metrological regions marked in Fig. 6d.

The second, the magnetic field condition, is a limiting factor for G/SiC for which the $\mu \approx 1$ m²V⁻¹s⁻¹ and $\mu B > 1$ conditions are fulfilled only for a magnetic field $B > 1$ T. In HgTe QW samples (mobility ~ 10 m²V⁻¹s⁻¹), this condition is fulfilled already at $B \geq 0.1$ T. One can see that the metrological range for HgTe QWs samples may be obtained in relatively lower magnetic fields.

The optimum $T \approx 1.5$ K metrological conditions for HgTe QWs are predicted with $d = 6.4$ nm ($\epsilon = -0.32\%$) and $d = 4.6$ nm ($\epsilon = 1.3\%$) for $B \approx 0.3$ T and $B \approx 0.5$ T, respectively. These QWs are hosting Dirac fermions with normal band ordering, ensuring maximum Landau level splitting and absence of topological edge conducting channels. Figure 6 clearly shows that HgTe based QWs

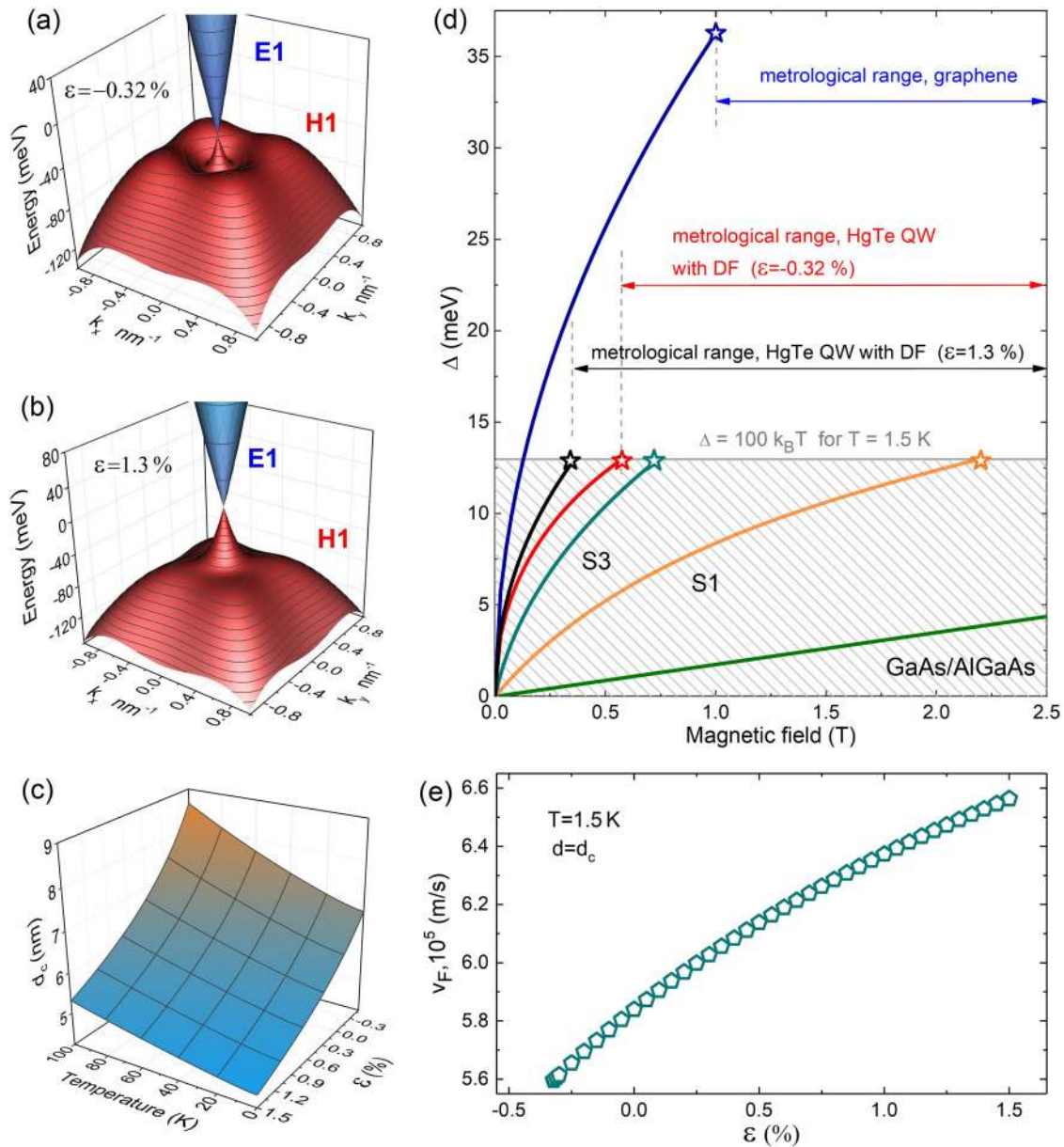


Fig. 6 **a, b** Calculated energy dispersions for two HgTe QWs hosting massless Dirac fermions for $d_c = 6.4$ nm, strain $\varepsilon = -0.32\%$ (CdTe buffer) and $d = 4.6$ nm, $\varepsilon = 1.3\%$, respectively. **c** Critical QW width d_c as a function of strain and temperature. **d** Energy gap Δ between two lowest LLs of the valence band at $\nu = -1$ as a function of the magnetic field for these two QWs (solid red and black curves, respectively) as well as for samples S1 (orange line) and S3 (cyan line); data for graphene (blue line) and GaAs/AlGaAs (green line) are also shown. The gray horizontal line is the lower boundary of the metrological range $\Delta \geq 100k_B T$ at $T = 1.5$ K. Vertical gray dashed lines indicate metrologically useful range where condition $\mu B \geq 1$ is fulfilled. Points at which two conditions starts execute marked by stars. **e** Band velocity v_F of massless Dirac fermions vs. strain

may be interesting for QHE standards developments because they may have graphene-like band structure (large Landau level splitting) and simultaneously they may host very high mobility carriers.

These considerations demonstrate that there is a considerable room for optimizing the performance and for demonstrating the practical relevance of resistance standards of HgTe quantum wells.

DISCUSSION

Although we show possibility to reach, using HgTe QWs, favorable cryomagnetic conditions for QHE metrology—the real metrological applications require some important developments. They are

very well illustrated by the work on graphene based QHE metrology sensors.^{22,29,52,55} The most important developments necessary in the case of HgTe QW are discussed below.

First of all—as stated in the main part of the paper—one has to grow narrower QWs with—direct (non-inverted band structure) and if possible with compressive strain that leads to enhancement of the Fermi velocity (enhanced Landau level splitting). But, to reach a metrological precision one needs not only non-inverted band structure QWs (avoiding edge channel parasitic conduction) but also provide samples operating with the highest possible current. The current can be increased by processing devices with bigger geometrical dimensions and with smaller contact resistance. This current is usually limited not only by the sample

geometry and contacts quality but also by carrier heating phenomena leading to QHE breakdown. Different carrier heating phenomena may be specific for each material depending on strength of electron–phonon interaction or phenomena of the charge transfer between the carriers and the reservoir.^{50,52} The research on the maximization of QHE breakdown current is surely one of the most important tasks—for future research on metrological applications of HgTe QWs.

In our experiments the highest precision of QHE resistance (in the 10^{-4}) was obtained. This precision is still far from being acceptable for metrological applications but we believe that it can be reached once mentioned above technological developments concerning correct band structure, sample geometry and contact resistance are successfully overcome.

To summarize, we have investigated the HgTe/(Cd,Hg)Te QWs in view of their application for new competitive QHE standards. We have shown that the coexistence of helical quantum spin Hall states and conventional chiral quantum Hall states in the topologically non-trivial region ($d > d_c$, $B < B_c$) may restrict the accuracy of the Hall resistance quantization. At the same time, our results demonstrate that for the non-inverted QWs close to the critical width d_c at which Dirac fermions control the charge transport and charge transfer mechanisms ensure wide plateaus (“charge reservoir” model), the QHE metrological conditions can be reached for holes (p-type samples) in very favorable cryomagnetic conditions: low magnetic fields (going even below 0.5 T) and at relatively high temperatures (going even above 1.5 K). These conditions are substantially more favorable than those required for the use of current QHE standards. Our experiments and realistic band structure calculations indicate a possibility for further improvements of the QHE metrological conditions in compressively strained HgTe/(Cd,Hg)Te QWs, for which the Fermi velocity is even higher. This opens the door for the development of QHE metrological devices operating with permanent magnets (without superconducting coils) and at liquid helium temperatures (without ^3He or dilution refrigerators). Accordingly, MBE-grown (Hg,Cd)Te-based QWs with Dirac fermions are semiconductor materials with prospects for a large scale fabrication and a wide use of QHE resistance standards devices by academic and industrial institutions. However, further work is needed to establish breakdown currents, to check long term stability and reproducibility as well as to compare quantization accuracy with other 2D systems under QHE conditions.⁵⁵

METHODS

The investigated structures were grown by molecular beam epitaxy (MBE) on semi-insulating GaAs substrate with [013] orientation. Samples S1, S2, and S3, HgTe quantum wells of 7.1, 8, and 6.5 nm thickness with barrier compositions of HgTe/Cd_{0.62}Hg_{0.38}Te, HgTe/Cd_{0.62}Hg_{0.38}Te, and HgTe/Cd_{0.65}Hg_{0.35}Te, respectively. Structures have been selectively doped with Indium and covered by 40 nm CdTe cap layer. For all samples low-temperature method of microstructurisation based on electron-beam lithography and wet chemical etching were used to produce a Hall bridge of dimensions $L \times W = 80 \times 20 \mu\text{m}^2$ and $L \times W = 40 \times 20 \mu\text{m}^2$ (samples S1 and S2, respectively) and $L \times W = 650 \times 50 \mu\text{m}^2$ (sample S3). After that we used ICP PECVD method to deposit dielectric 160 and 200 nm Si₃N₄ dielectric on the surface of samples S2 and S3, respectively. During last step of processing, gate electrode (150 nm Ti/Au metallic layer) was thermally deposited on top of the samples. Contacts were performed by Indium soldering. The magnetotransport experiments have been carried out using the 8 T superconducting magnet system and standard lock-in measurement techniques. High-precision resistance measurements were performed using an HP3458A multimeter. In order to avoid sample heating current in range of 10 nA–1 μA was applied.

The cross section of GaAs/ZnTe/CdTe/(Cd,Hg)Te heterostructures was prepared with FEI Helios 600 Nanolab dual beam FIB. Protective Pt layer was deposited from metalorganic source with the use of 15 kV electrons and 30 kV Ga ions. Final thinning of transparent for electron lamella was performed at 2 kV. TEM investigations were performed in STEM and TEM

mode using FEI Titan 80-300 microscope equipped with the image corrector operating at 300 kV.

DATA AVAILABILITY

The data that support the findings of this study are available from the corresponding authors on request.

ACKNOWLEDGEMENTS

The research in Poland was partially supported by the Foundation for Polish Science through the IRA Program financed by EU within SG OP Program and No. TEAM/2016-3/25, by the National Science Centre, Poland, decisions No. DEC-2011/02/A/ST3/00125, 2013/10/M/ST3/00705, UMO-2015/17/N/ST3/02314, 2016/22/E/ST7/00526, and UMO-2017/25/N/ST3/00408. The authors also acknowledge Russian Foundation for Basic Research (Grants 15-52-16008 and 16-02-00672), ARPE Terasens project and Terahertz Platform both provided by Occitanie Region. The theoretical calculations for the compressively strained QWs were performed in the framework of project 16-12-10317, supported by the Russian Science Foundation. S.K. and A.K. acknowledge the Russian Ministry of Education and Science (MK-1136.2017.2 and SP-5051.2018.5). The authors gratefully thank Z.D. Kvon from the Institute of Semiconductor Physics (Siberian Branch, Russian Academy of Sciences) for stimulating and fruitful discussions as well as for providing the processed gated Hall bar samples.

AUTHOR CONTRIBUTIONS

I.Y., G.G., B.J., C.C., W.D., A.M.K., D.B.B. and G.G. have contributed to the experiments. The sample growth was performed by S.A.D. and N.N.M. The sample processing and TEM investigations were performed by M.M., J.W. and S.K. Theoretical calculations were made by S.S.K., K.E.S., V.I.G. and T.D. All co-authors have participated in the discussion of the data. The paper and supplementary information were written by W. K., I.Y., S.S.K., G.G., T.D., F.T. and B.J.

ADDITIONAL INFORMATION

Supplementary Information accompanies the paper on the *npj Quantum Materials* website (<https://doi.org/10.1038/s41535-019-0154-3>).

Competing interests: The authors declare no competing interests.

Publisher's note: Springer Nature remains neutral with regard to jurisdictional claims in published maps and institutional affiliations.

REFERENCES

- Dornhaus, R., Nimtz, G. & Schlicht, B. *Narrow-Gap Semiconductors*. (Springer, Berlin, Heidelberg, 1983).
- Gałazka, R. R. & Sosnowski, L. Conduction Band Structure of Cd_{0.1}Hg_{0.9}Te. *Phys. Stat. Sol.* **20**, 113–120 (1967).
- Orlita, M. et al. Observation of three-dimensional massless Kane fermions in a zinc-blende crystal. *Nat. Phys.* **10**, 233–238 (2014).
- Tepe, F. et al. Temperature-driven massless Kane fermions in HgCdTe crystals. *Nat. Commun.* **7**, 12576 (2016).
- Dubowski, J., Dietl, T., Szymańska, W. & Gałazka, R. Electron scattering in Cd_xHg_{1-x}Te. *J. Phys. Chem. Solids* **42**, 351–362 (1981).
- Ruffenach, S. et al. HgCdTe-based heterostructures for Terahertz photonics. *APL Mater.* **5**, 035503 (2017).
- Rogalski, A., Martyniuk, P. & Kopytko, M. Challenges of small-pixel infrared detectors: a review. *Rep. Prog. Phys.* **79**, 046501 (2016).
- Morozov, S. et al. Stimulated emission from HgCdTe quantum well heterostructures at wavelengths up to 19.5 μm . *Appl. Phys. Lett.* **111**, 192101 (2017).
- König, M. et al. Quantum spin Hall insulator state in HgTe quantum wells. *Science* **318**, 766–770 (2007).
- König, M. et al. The quantum spin Hall effect: theory and experiment. *J. Phys. Soc. Jpn.* **77**, 031007 (2008).
- Brüne, C. et al. Quantum Hall effect from the topological surface states of strained bulk HgTe. *Phys. Rev. Lett.* **106**, 126803 (2011).
- Qi, X.-L. & Zhang, S.-C. Topological insulators and superconductors. *Rev. Mod. Phys.* **83**, 1057–1110 (2011).
- Ortmann, F., Roche, S. & Valenzuela, S. O. *Topological Insulators: Fundamentals and Perspectives*. (John Wiley & Sons, Hoboken, 2015).
- Büttner, B. et al. Single valley Dirac fermions in zero-gap HgTe quantum wells. *Nat. Phys.* **7**, 418–422 (2011).

15. Krishtopenko, S. S., Knap, W. & Teppe, F. Phase transitions in two tunnel-coupled HgTe quantum wells: bilayer graphene analogy and beyond. *Sci. Rep.* **6**, 30755 (2016).
16. Piotrowski, J. & Rogalski, A. *High-Operating Temperature Infrared Photodetectors*. (SPIE Press, Bellingham, WA, 2007).
17. Dvoretzky, S. et al. Growth of HgTe quantum wells for IR to THz detectors. *J. Electron. Mater.* **39**, 918–923 (2010).
18. Klitzing, K. v., Dorda, G. & Pepper, M. New method for high-accuracy determination of the fine-structure constant based on quantized Hall resistance. *Phys. Rev. Lett.* **45**, 494–497 (1980).
19. Tong, D. *Lectures on the Quantum Hall Effect*. <https://arxiv.org/abs/1606.06687> (2016).
20. Poirier, W. & Schopfer, F. Resistance metrology based on the quantum Hall effect. *Eur. Phys. J.: Spec. Top.* **172**, 207–245 (2009).
21. Jeckelmann, B. & Jeanneret, B. The quantum Hall effect as an electrical resistance standard. *Rep. Prog. Phys.* **64**, 1603–1655 (2001).
22. Janssen, T. J. B. M., Tzalenchuk, A., Lara-Avila, S., Kubatkin, S. & Fal'ko, V. I. Quantum resistance metrology using graphene. *Rep. Prog. Phys.* **76**, 104501 (2013).
23. Taylor, B. N. & Witt, T. J. New international electrical reference standards based on the Josephson and quantum Hall effects. *Metrologia* **26**, 47–62 (1989).
24. Chang, C.-Z. et al. Experimental observation of the quantum anomalous Hall effect in a magnetic topological insulator. *Science* **340**, 167–170 (2013).
25. Fox, E. J. et al. Part-per-million quantization and current-induced breakdown of the quantum anomalous Hall effect. *Phys. Rev. B* **98**, 075145 (2018).
26. Götz, M. et al. Precision measurement of the quantized anomalous Hall resistance at zero magnetic field. *Appl. Phys. Lett.* **112**, 072102 (2018).
27. Parmentier, F. D. et al. Quantum Hall effect in epitaxial graphene with permanent magnets. *Sci. Rep.* **6**, 38393 (2016).
28. Ribeiro-Palau, R. et al. Quantum Hall resistance standard in graphene devices under relaxed experimental conditions. *Nat. Nanotechnol.* **10**, 965–971 (2015).
29. Janssen, T. J. B. M. et al. Operation of graphene quantum Hall resistance standard in a cryogen-free table-top system. *2D Mater.* **2**, 035015 (2015).
30. Lafont, F. et al. Quantum Hall resistance standards from graphene grown by chemical vapour deposition on silicon carbide. *Nat. Commun.* **6**, 6806 (2015).
31. Novoselov, K. S. et al. Room-temperature quantum Hall effect in graphene. *Science* **315**, 1379 (2007).
32. Lara-Avila, S. et al. Non-volatile photochemical gating of an epitaxial graphene/polymer heterostructure. *Adv. Mater.* **23**, 878–882 (2011).
33. Yang, M. et al. Puddle-induced resistance oscillations in the breakdown of the graphene quantum Hall effect. *Phys. Rev. Lett.* **117**, 237702 (2016).
34. Kozlov, D. A., Kvon, Z. D., Mikhailov, N. N. & Dvoretzky, S. A. Quantum Hall effect in a system of gapless Dirac fermions in HgTe quantum wells. *JETP Lett.* **100**, 724–730 (2015).
35. Kozlov, D. et al. Quantum Hall effect in HgTe quantum wells at nitrogen temperatures. *Appl. Phys. Lett.* **105**, 132102 (2014).
36. Khouri, T. et al. High-temperature quantum Hall effect in finite gapped HgTe quantum wells. *Phys. Rev. B* **93**, 125308 (2016).
37. Vaimann, T., Kallaste, A., Kilk, A. & Belahcen, A. Magnetic properties of reduced Dy NdFeB permanent magnets and their usage in electrical machines. *IEEE Xplore* <https://doi.org/10.1109/AFRCON.2013.6757787> (2014).
38. Richardson, R. C. & Smith, E. N. *Experimental Techniques in Condensed Matter Physics at Low Temperatures*. (Advanced Book Classics, USA, 2018).
39. Giesbers, A. J. M. et al. Quantum resistance metrology in graphene. *Appl. Phys. Lett.* **93**, 222109–222112 (2008).
40. Guignard, J., Leprat, D., Glattli, D. C., Schopfer, F. & Poirier, W. Quantum Hall effect in exfoliated graphene affected by charged impurities: metrological measurements. *Phys. Rev. B* **85**, 165420 (2012).
41. Rigosi, A. F. et al. Graphene devices for tabletop and high current quantized hall resistance standards. *IEEE Proceedings* <https://doi.org/10.1109/TIM.2018.2882958> (2018).
42. Majewicz, M. et al. Low temperature processing of nanostructures based on II–VI semiconductors quantum wells. *Acta Phys. Pol. A* **126**, 1174–1176 (2014).
43. Krishtopenko, S. S. et al. Pressure- and temperature-driven phase transitions in HgTe quantum wells. *Phys. Rev. B* **94**, 245402 (2016).
44. Kadykov, A. M. et al. Temperature-induced topological phase transition in HgTe quantum wells. *Phys. Rev. Lett.* **120**, 086401 (2018).
45. Marcinkiewicz, M. et al. Temperature-driven single-valley Dirac fermions in HgTe quantum wells. *Phys. Rev. B* **96**, 035405 (2017).
46. Zholudev, M. et al. Magnetospectroscopy of two-dimensional HgTe-based topological insulators around the critical thickness. *Phys. Rev. B* **86**, 205420 (2012).
47. Chen, J.-C., Wang, J. & Sun, Q.-F. Effect of magnetic field on electron transport in HgTe/CdTe quantum wells: numerical analysis. *Phys. Rev. B* **85**, 125401 (2012).
48. Ma, E. Y. et al. Unexpected edge conduction in mercury telluride quantum wells under broken time-reversal symmetry. *Nat. Commun.* **6**, 7252 (2015).
49. Grabecki, G. et al. Nonlocal resistance and its fluctuations in microstructures of band-inverted HgTe/(Hg,Cd)Te quantum wells. *Phys. Rev. B* **88**, 165309 (2013).
50. Zawadzki, W., Raymond, A. & Kubisa, M. Reservoir model for two-dimensional electron gases in quantizing magnetic fields: a review. *Phys. Status Solidi B* **251**, 247–262 (2014).
51. Kopylov, S., Tzalenchuk, A., Kubatkin, S. & Fal'ko, V. I. Charge transfer between epitaxial graphene and silicon carbide. *Appl. Phys. Lett.* **97**, 112109 (2010).
52. Janssen, T. J. B. M. et al. Anomalously strong pinning of the filling factor $\nu=2$ in epitaxial graphene. *Phys. Rev. B* **83**, 233402 (2011).
53. Leubner, P., Lunczer, L., Brüne, C., Buhmann, H. & Molenkamp, L. W. Strain engineering of the band gap of HgTe quantum wells using superlattice virtual substrates. *Phys. Rev. Lett.* **117**, 086403 (2016).
54. Krishtopenko, S. S. & Teppe, F. Realistic picture of helical edge states in HgTe quantum wells. *Phys. Rev. B* **97**, 165408 (2018).
55. Janssen, T. J. B. M. et al. Precision comparison of the quantum Hall effect in graphene and gallium arsenide. *Metrologia* **49**, 294–306 (2012).



Open Access This article is licensed under a Creative Commons Attribution 4.0 International License, which permits use, sharing, adaptation, distribution and reproduction in any medium or format, as long as you give appropriate credit to the original author(s) and the source, provide a link to the Creative Commons license, and indicate if changes were made. The images or other third party material in this article are included in the article's Creative Commons license, unless indicated otherwise in a credit line to the material. If material is not included in the article's Creative Commons license and your intended use is not permitted by statutory regulation or exceeds the permitted use, you will need to obtain permission directly from the copyright holder. To view a copy of this license, visit <http://creativecommons.org/licenses/by/4.0/>.

© The Author(s) 2019